

## ARTICLE OPEN



# Ultra-broad spectral photo-response in FePS<sub>3</sub> air-stable devices

Maria Ramos<sup>1</sup>✉, Felix Carrascoso<sup>2</sup>, Riccardo Frisenda<sup>2</sup>, Patricia Gant<sup>2</sup>, Samuel Mañas-Valero<sup>3</sup>, Dorye L. Esteras<sup>3</sup>, José J. Baldoví<sup>3</sup>, Eugenio Coronado<sup>3</sup>, Andres Castellanos-Gomez<sup>2</sup>✉ and M. Reyes Calvo<sup>1,4</sup>✉

Van der Waals materials with narrow energy gaps and efficient response over a broadband optical spectral range are key to widen the energy window of nanoscale optoelectronic devices. Here, we characterize FePS<sub>3</sub> as an appealing narrow-gap p-type semiconductor with an efficient broadband photo-response, a high refractive index, and a remarkable resilience against air and light exposure. To enable fast prototyping, we provide a straightforward guideline to determine the thickness of few-layered FePS<sub>3</sub> nanosheets extracted from the optical transmission characteristics of several flakes. The analysis of the electrical photo-response of FePS<sub>3</sub> devices as a function of the excitation energy confirms a narrow gap suitable for near IR detection (1.23 eV) and, more interestingly, reveals a broad spectral responsivity up to the ultraviolet region. The experimental estimate for the gap energy is corroborated by ab-initio calculations. An analysis of photocurrent as a function of gate voltage and incident power reveals a photo-response dominated by photogating effects. Finally, aging studies of FePS<sub>3</sub> nanosheets under ambient conditions show a limited reactivity of the outermost layers of flakes in long exposures to air.

npj 2D Materials and Applications (2021)5:19; <https://doi.org/10.1038/s41699-021-00199-z>

## INTRODUCTION

Two-dimensional crystals (2D materials), owning strong in-plane covalent bonds and weak van der Waals interlayer interactions, have attracted big attention since the isolation of graphene sheets by exfoliation of bulk graphite<sup>1</sup>. The simplicity and rapid prototyping provided by the Scotch tape technique together with the wide range of properties covered by these materials has opened an enormous research field with the potential to have an impact on a diverse number of applications. Because of the lack of bandgap in graphene, its direct application in digital electronics and optoelectronics is limited. Beyond graphene, the family of transition metal dichalcogenides (TMDCs) has been of great interest for optoelectronic applications owing to their intrinsic bandgap in the visible range and their strong luminescent excitonic features<sup>2–4</sup>. However, the large bandgap of TMDCs (in the 1.5–2 eV range) limits their application exclusively to the visible part of the electromagnetic spectrum. Finding materials with a wider spectral sensitivity at the two-dimensional level could expand the number of applications of van der Waals materials, from solar photodetection at the ultraviolet–visible (UV–VIS) spectral range to night imaging and remote sensing at the near-infrared (NIR)<sup>5,6</sup>.

Broadening the detection window at the 2D level requires the study of van der Waals materials with smaller bandgap values, to access the NIR part of the spectrum, and simultaneously keeping enough photo-response over a wide range of energies above the bandgap. Recently, transition metal chalcogenophosphates (TMCPs), with general formula MPX<sub>3</sub> (with M a transition metal, P phosphorus and X = S or Se chalcogens), have attracted great attention from the 2D material science community since they are easy to exfoliate, presenting cleavage energy even smaller than graphite<sup>7</sup>. Although little is still known about the optoelectronic properties of this emergent family of 2D materials, few works have

already proposed field-effect devices based on few-layered TMCPs as UV photodetectors<sup>8–10</sup>. Whereas MnPS<sub>3</sub> is a wide gap semiconductor with bandgap energy in the UV range in its bulk form<sup>11</sup>, the large UV responsivity reported for NiPS<sub>3</sub><sup>9</sup> and FePS<sub>3</sub><sup>10</sup> is somehow unexpected since these are materials that, in bulk, present a bandgap edge in the NIR region<sup>9</sup>. Since reports on the photo-response of narrow gap TMCPs over a wide range of wavelengths are scarce, a preliminary optoelectronic study of these materials could pave the way toward new 2D broadband optoelectronic devices. In addition to the promising properties for broadband photodetection, FePS<sub>3</sub> and other magnetic TMCPs exhibit antiferromagnetic order when cooled down below their Néel temperatures, which are in the range 85–150 K<sup>12–15</sup>. The intrinsic magnetic order of FePS<sub>3</sub> makes it an appealing material for applications in magneto-optics and 2D spintronics<sup>16–18</sup>.

Here, we present a comprehensive characterization of optical, optoelectronic, and stability properties of FePS<sub>3</sub> nanosheets. First, we propose an optical microscopy-based method to identify the thickness of few-layer FePS<sub>3</sub> sheets deposited onto transparent polymeric stamps. The quantitative analysis of optical microscopy images of FePS<sub>3</sub> flakes also allows us to estimate their refractive index, a very important property to design future optical and optoelectronic devices based on FePS<sub>3</sub> nanosheets. We also report on the photo-response of a few-layer FePS<sub>3</sub> field-effect device in the UV–VIS–NIR spectral range and we determine the bandgap of this material toward the two-dimensional limit. Ab-initio calculations support the experimental findings and provide further insight into the magnitude of electronic interactions on this material. Finally, we study the environmental stability of FePS<sub>3</sub> flakes under ambient conditions through optical, electrical, and optoelectronic measurements over time. The properties of flakes of FePS<sub>3</sub> seem stable over time of hours but aging effects appear over days exposure to air.

<sup>1</sup>Departamento de Física Aplicada, Universidad de Alicante, Alicante, Spain. <sup>2</sup>Materials Science Factory, Instituto de Ciencia de Materiales de Madrid (ICMM-CSIC), Madrid, Spain.

<sup>3</sup>Instituto de Ciencia Molecular (ICMol), Universitat de València, Paterna, Spain. <sup>4</sup>Instituto Universitario de Materiales de Alicante (IUMA), Universidad de Alicante, Alicante, Spain.

✉email: mramos@ua.es; andres.castellanos@csic.es; reyes.calvo@ua.es

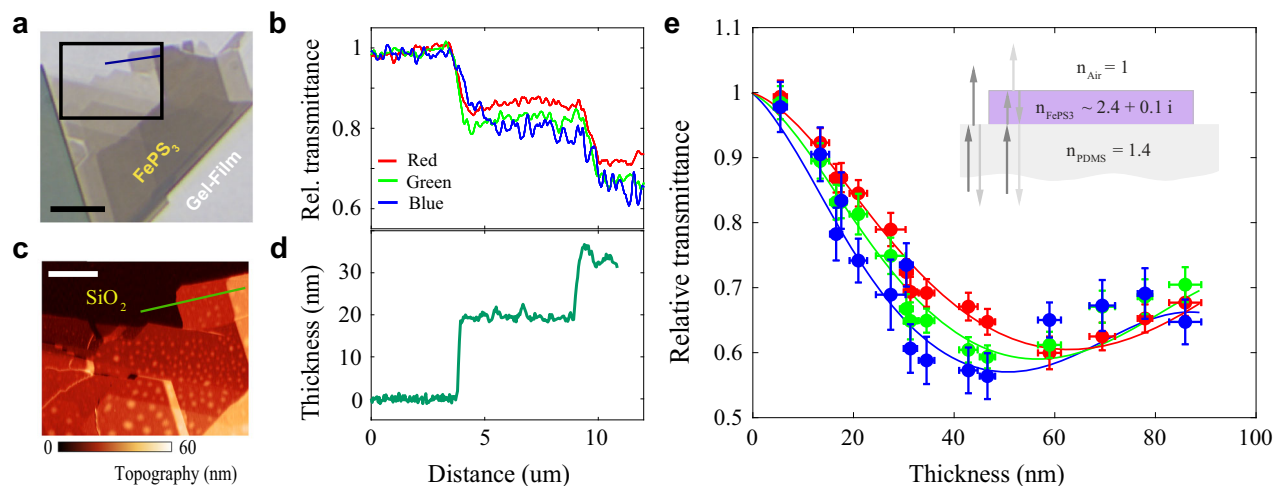


**Fig. 1 Transmittance and thickness characterization.** **a** White-light optical transmission image of a FePS<sub>3</sub> flake deposited onto a transparent polymeric substrate. The black scale bar represents 10  $\mu\text{m}$ . The flake appears quartered in stairs or terraces which correspond to different material thicknesses and appear as different value steps in the **b** transmission intensity line profiles for the red, green, and blue channels of the CMOS camera, normalized to the corresponding transmission intensities at the bare substrate (relative transmission) along the path marked as a dark blue line in **(a)**. **c** AFM topography image of a small section of the flake shown in **(a)** after its deposition onto a SiO<sub>2</sub>/Si substrate. The white scale bar indicates 5  $\mu\text{m}$ . **d** Thickness profile along the path marked with a green line in **(c)**. **e** Relative transmittance versus thickness of FePS<sub>3</sub> nanosheets extracted from the comparison of optical and AFM characterization data for several flakes. The red, green, and blue dots correspond to the experimental data points for the corresponding RGB channels, whereas the red, green, and blue line curves are the simulated results from the transfer-matrix model (sketched in the inset).

## RESULTS AND DISCUSSION

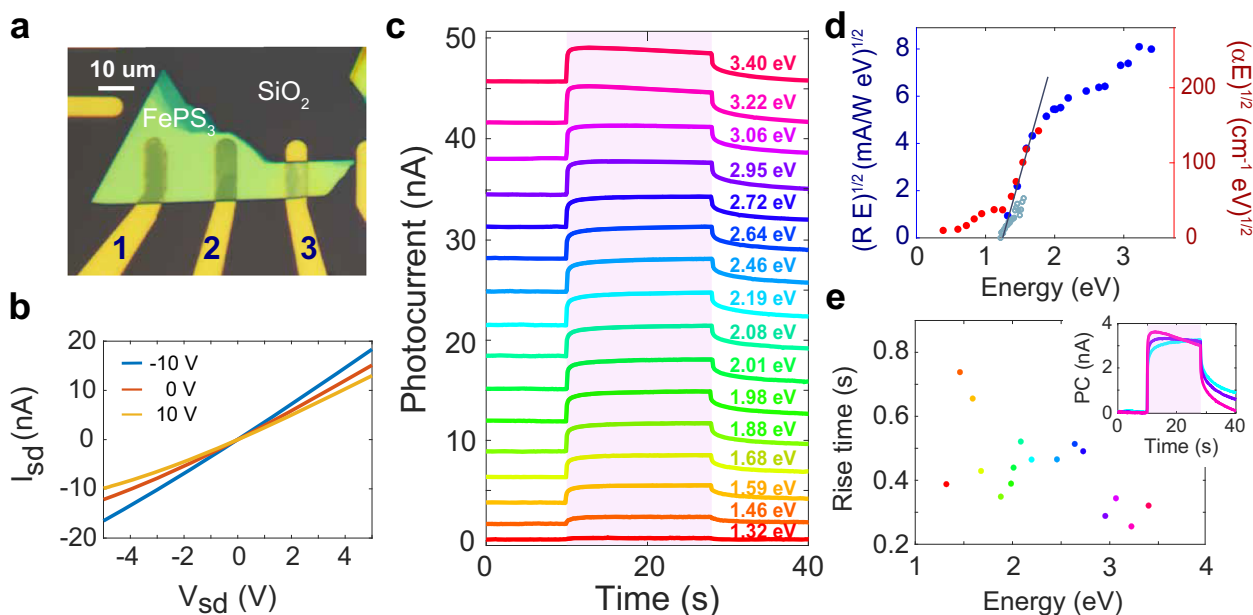
### Thickness identification and refractive index estimation

Figure 1a shows a transmission mode optical microscopy image of an exfoliated FePS<sub>3</sub> flake with a different number of layers deposited onto a Gel-Film polymeric substrate. A very simple method to estimate the thickness of layered material flakes consists in the comparison of the relative transmittance images<sup>19</sup> through their comparison to atomic force microscopy (AFM) topography maps. The transmittance variations in the optical images associated with changes in material thickness can be clearly identified in the intensity line profiles for the red, green, and blue (RGB) channels of the digital camera. For example, from the line profiles shown in Fig. 1b, three different levels of transmission are identified for each RGB curve along the path marked in Fig. 1a, corresponding to changes in material thickness or number of layers. The transmittance data in the RGB curves are normalized to the intensity of the transparent substrate at the respective channel. Figure 1c illustrates an AFM image of a small section of the FePS<sub>3</sub> flake shown in Fig. 1a (area delimited within the black square) deposited onto a SiO<sub>2</sub>/Si substrate. The comparison of transmittance and AFM topography data for the same areas of given flakes allows the mapping between relative transmittance and thickness data. As an example, this can be observed in the line profile of Fig. 1d, extracted from the AFM data (Fig. 1c) and crossing approximately the same area of flake terraces explored in transmittance (Fig. 1b). Three different heights are clearly observed from left to right in the AFM profile: 0 nm (the line is on the SiO<sub>2</sub>/Si substrate), 20 nm (the line is on the FePS<sub>3</sub> nanosheet), and 35 nm (the line is on a thicker terrace of the same FePS<sub>3</sub> flake). These values can be now associated with the three optical transmission levels observed for each of the RGB channels in the line profiles of Fig. 1b.

Following the sequence of measurements detailed above, the acquisition of optical transmission images and AFM images for several flakes with different thicknesses has allowed to build up a straightforward guide for the identification of FePS<sub>3</sub> nanosheet thicknesses (Fig. 1e). The feasibility of using this method is determined by the horizontal/vertical error-bars accompanying each data point, indicating the standard deviations for each

thickness/transmittance measurement, respectively (see Supplementary Note 1 for more details). Even if non-monotonic, transmittance curves for the three RGB channels present minima at different thickness values, allowing for an unambiguous estimation of flake thickness, with a maximum error of  $\pm 10$  nm, by comparing the transmittance value of the three channels. The thickness identification methodology proposed in Fig. 1e permits to skip time-consuming AFM measurements and to proceed right away from a simple optical microscopy image to the deterministic placement of the FePS<sub>3</sub> flake of interest onto the desired substrate for the assembly of 2D FePS<sub>3</sub>-based nanodevices.

The occurrence of a minimum of transmittance at about 40–60 nm thickness for the three channels hints at an oscillatory behavior due to constructive interference of light within the material, while the overall decay of transmitted intensity with increasing thickness indicates light being absorbed as it travels through the material. The experimental data points in Fig. 1e can be simulated using the transfer matrix method to calculate the Fresnel coefficients for absorption, reflection, and transmission of light at each layer and optical interface, respectively<sup>20</sup>. In our model, we consider the case of normal light incidence to a layer of FePS<sub>3</sub> sandwiched between two semi-infinite media: air and Gel-Film, with real refractive indices of  $n_0 = 1$  and  $n_1 = 1.43$ , respectively, and constant for the range of wavelengths considered. Note that the refractive index value for the Gel-Film substrate has been chosen as that of polydimethylsiloxane (PDMS)<sup>21</sup>. FePS<sub>3</sub> is assumed to have both real and imaginary contributions to the refractive index ( $n_2 = a + ib$ ). In the model, the estimated transmittance for each channel is averaged over the channel bandwidth, weighted to the quantum efficiency of the CMOS sensor at the corresponding wavelength values. Fits of our experimental data to the model yield estimated values of the real part of the refractive index of FePS<sub>3</sub> equal to  $a \approx 2.45$  for all RGB channels and of the imaginary part (extinction coefficient) equal to 0.06, 0.09, and 0.13 for the red, green and blue channel datasets, respectively (See Supplementary Note 2 for a validation test of this estimate). The estimated real refractive index value for FePS<sub>3</sub> is in close similarity to the one reported for its alike TMCP based on manganese, MnPS<sub>3</sub>, presenting a value of 2.41<sup>22</sup>.



**Fig. 2 Electrical and photo-response characterization.** **a** Optical image of device A (30-nm thick) transferred onto a SiO<sub>2</sub> (300 nm)/Si substrate with pre-patterned Ti/Au (10 nm/40 nm) contacts (1–3). **b** Two-terminal source-drain  $I$ - $V$  characteristics for different values of the applied gate voltage ( $V_g = -10, 0, 10$  V), measured between contacts labeled 1 and 2 in **(a)**. The increase of current for negative values of  $V_g$  shows the p-type nature of FePS<sub>3</sub>. **c** Photocurrent versus time for different optical LED energies ranging from NIR (1.32 eV) to UV (3.40 eV). The shaded area indicates the time when light is ON. The dark current has been subtracted to the values of the drain current during illumination ( $I_{ph} = I_{light} - I_{dark}$ ) for each energy curve. The curves have been vertically offset for clarity. The responsivity of device A extracted from the photocurrent data is represented in **(d)** as an experimental Tauc plot in blue dots, together with a higher resolution set of data (gray dots) and with absorbance measurements of FePS<sub>3</sub> extracted from Brec et al. (red dots) for comparison<sup>11</sup>. The gap energy is determined by the crossing of the linear fit to the responsivity data (black line) with the  $x$ -axis. **e** Rise time of the FePS<sub>3</sub> phototransistor as a function of different incident energies. The inset compares the trend of the photocurrent over time at low ( $E = 2.19$  eV, in cyan), medium ( $E = 2.95$  eV, in purple) and high energies ( $E = 3.22$  eV, in magenta).

### Spectral photo-response and gap energy determination

Making use of the thickness identification guide provided in Fig. 1e, new FePS<sub>3</sub> flakes were exfoliated and deposited on a Gel-Film substrate to directly search for a flake with a homogeneous thickness of ~30–50 nm and elongated geometry. The transparency of the Gel-Film substrate allowed for an accurate alignment of the identified flakes in order to be transferred onto a SiO<sub>2</sub>/Si substrate with pre-patterned Ti/Au contacts. Figure 2a shows an optical image of a field-effect device with a ~30-nm-thick FePS<sub>3</sub> channel (device A). Source-drain  $I$ - $V$  curves have been recorded under different gate bias voltages. The application of negative gate voltages results in an increase of the electrical current passing through the FePS<sub>3</sub> flake (Fig. 2b), as expected from the p-doped character reported for FePS<sub>3</sub> bulk crystals<sup>23</sup> (see Supplementary Note 3, where  $I_{sd}$ - $V_{sd}$  curves for a larger range of  $V_g$  values are presented in a similar device). The low abundance of p-type layered semiconductors makes FePS<sub>3</sub> an attractive alternative for stacking in p-n heterojunctions and of particular interest in this case for the study of magnetic proximity effects<sup>24</sup>.

The response to light of device A is characterized at different energies ranging from the NIR (1.32 eV) to the UV (3.40 eV) region of the electromagnetic spectrum using a selection of light-emitting diodes (LEDs) (Fig. 2c). Here, photoexcited carriers contribute to the electrical current in presence of an electric field created by a constant source-drain voltage  $V_{sd} = 5$  V and zero gate bias. During illumination at different energies, the light carries a constant power density  $P_{LED} = 49.5$  mW cm<sup>-2</sup>.

As it can be deduced from Fig. 2c, the photocurrent, calculated as  $I_{ph} = I_{light} - I_{dark}$ , rises as we increase the energy up to 2 eV, stays roughly constant up to 3 eV, and, interestingly, increases again for larger incident optical energies belonging to the UV spectrum. Moreover, our device responds to light in the entire

range of incident energies, evidencing that FePS<sub>3</sub> based nanodevices can be operated from the NIR part of the spectrum and going through the visible and UV spectral regions. The ultra-broadband characteristic of FePS<sub>3</sub> is of great relevance since many van der Waals materials present larger energy gaps and its use is limited to a narrower part of the electromagnetic spectrum. Recently, it has been also shown that a similar van der Waals magnetic material, CrSiTe<sub>3</sub>, presents ultrabroad wavelength photo-response<sup>25</sup>.

The responsivity of the device, calculated as the ratio of the generated photocurrent and the effective incident optical power ( $P_{eff} = P_{LED} A_{device} / A_{spot}$ ), is enhanced for increased photon energies, with values up to 20.3 mA W<sup>-1</sup> when illuminating at 3.22 eV (385 nm) and corresponding to an external quantum efficiency of ~7%. Similar responsivity trends with incident optical energy are obtained for other devices with slightly different thicknesses (see Supplementary Note 4 for device B with 50 nm FePS<sub>3</sub> thickness). The increase in responsivity at larger energies is in agreement with the increase in optical absorption of FePS<sub>3</sub> flakes at shorter wavelengths reported by Gao et al.<sup>10</sup>, although our data yields a lower responsivity in comparison to their results. The discrepancy between results may arise from the use of different device fabrication methods. On the one hand, the lithography process might affect the intrinsic carrier density and therefore the conductivity of the material. On the other hand, the choice of electrode metal, Au in our case versus Ti or Cr in other works, may increase the contact resistance and result in a lower two-terminal current.

Since the reported electronic and optical bandgap values of FePS<sub>3</sub> vary among different published works<sup>10,11</sup>, here we infer the optical bandgap energy  $E_g$  of the 30-nm thick FePS<sub>3</sub> nanosheet from the cut-off energy obtained in a linear fit to the responsivity

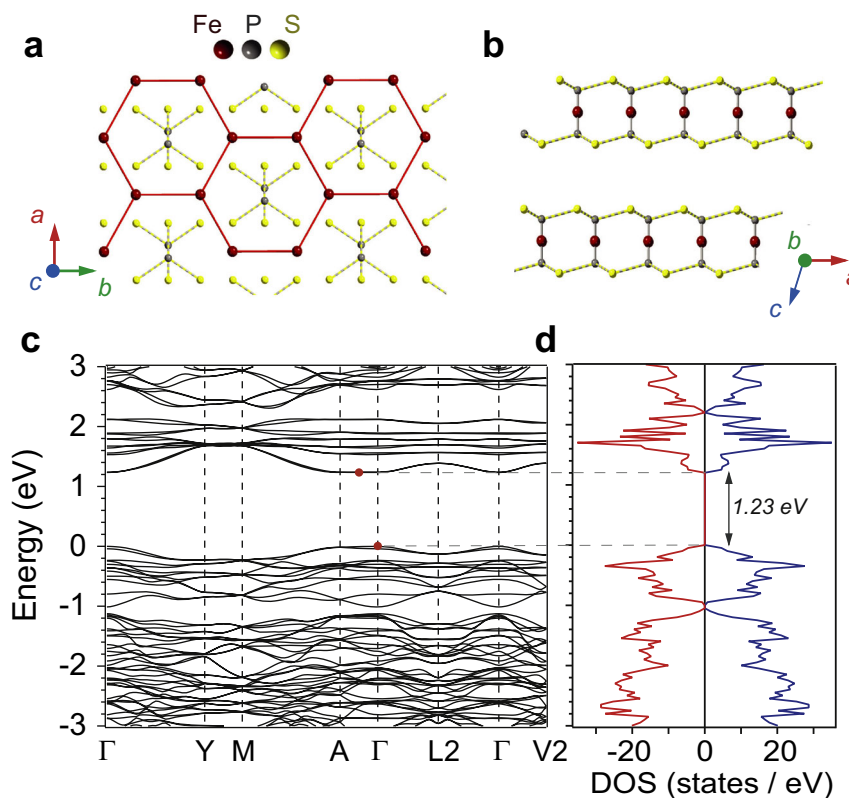


**Fig. 3** **Calculated band structure and DOS.** **a** Top view and **b** side view of the crystal structure of FePS<sub>3</sub>. Fe<sup>2+</sup> ions form a honeycomb lattice, enclosed by the (P<sub>2</sub>S<sub>6</sub>)<sup>4-</sup> bipyramids. The stacking of the layers of the monoclinic crystal structure is shown. Calculated GGA + D2 + *U* **c** band structure and **d** density of states: spin up (blue) and spin-down (red). The maximum and minimum of the valence and conduction bands respectively are marked with red dots defining the indirect energy gap.

data in a Tauc plot representation. Assuming that our device photocurrent arises from an indirect bandgap transition<sup>11,23</sup>, the Tauc plot constructed with the dataset presented in Fig. 2c results in the blue color markers of Fig. 2d. The point where a linear fit to the experimental data cuts the zero responsivity yields an estimate of  $E_g = 1.23$  eV. Photocurrent measurements using a Xenon white-light source integrated with a monochromator (Bentham) provide an improved energy resolution within the range of interest. The results, illustrated in the Tauc plot of Fig. 2d and represented by gray color markers, confirm the optical bandgap value previously obtained with the bench of LEDs. In addition to our experimental data, bulk FePS<sub>3</sub> absorbance measurements have been extracted from a work published by Brec et al.<sup>11</sup> and integrated in our Tauc plot as red color markers. It can be observed that our experimental results, based on the photocurrent response of the device, are in good agreement with the optical absorption measurements provided by Brec et al., except for energies below  $\sim 1.32$  eV, where *d-d* transitions dominate the absorption spectrum. These *d-d* transitions are attributed to the presence of iron in the compound and, being intra gap transitions, although contribute to the total absorption they are not expected to contribute to the photocurrent generation.

Upon LED modulation, the response speed of the device to the incident excitation has been calculated by following the 10–90% rise time for each illumination energy. To do so, the maximum photocurrent value has been chosen within the first 1.5 s after switching the LED ON, in order to discard the slower contributions to the photocurrent. Figure 2e shows the response time of the device as a function of the excitation energy. An average response time of  $\sim 440$  ms for all the energies has been measured. The photodetector responds faster for higher photon energies,

with a minimum rise time of 260 ms at 3.22 eV (385 nm). This response time is about two times slower than the rise times previously reported for field-effect devices based on FePS<sub>3</sub> nanosheets<sup>10,26</sup>. This could be also related to the effect of having different metal–semiconductor junctions. The photocurrent dynamics upon switching off the LEDs reveal longer relaxation tails for higher excitation energies, possibly originated from the detrapping of hot carriers traps and surface defects (see Supplementary Note 5).

The trend of the photocurrent upon illumination changes both in magnitude (Fig. 2d) and in time response (Fig. 2e) above 3 eV. The response of the device in the UV range is stronger and faster than for the IR and visible regimes. This could be related to the activation of hot carrier traps and defects proposed in the work of Ou et al.<sup>26</sup>, although further studies would be needed to fully understand this behavior. Zoom into the data is presented in the inset of Fig. 2e, revealing that the evolution of the photocurrent with time differs from a common case. Below 3 eV, photocurrent increases most of its value over the rise time and then slowly saturates toward a maximum value. Above 3 eV, after a more sudden and larger increase, the photocurrent slowly decreases with time. This could be related to a combination of positive and negative photoconductivity phenomena, such as those previously reported<sup>10,26</sup>.

In order to contrast and rationalize our experimental findings, we performed spin-polarized first-principles calculations based on density functional theory (DFT) as implemented in the Quantum Espresso code<sup>27</sup> (see “Methods”). Bulk FePS<sub>3</sub> presents a monoclinic unit cell with space group C2/m ( $a = 5.947$  Å,  $b = 10.300$  Å,  $c = 6.722$  Å, and  $\beta = 107.16^\circ$ ). In each layer of this van der Waals material, the Fe<sup>2+</sup> ions form a honeycomb that is surrounded by covalent (P<sub>2</sub>S<sub>6</sub>)<sup>4-</sup> bipyramids (Fig. 3a, b). We have investigated the

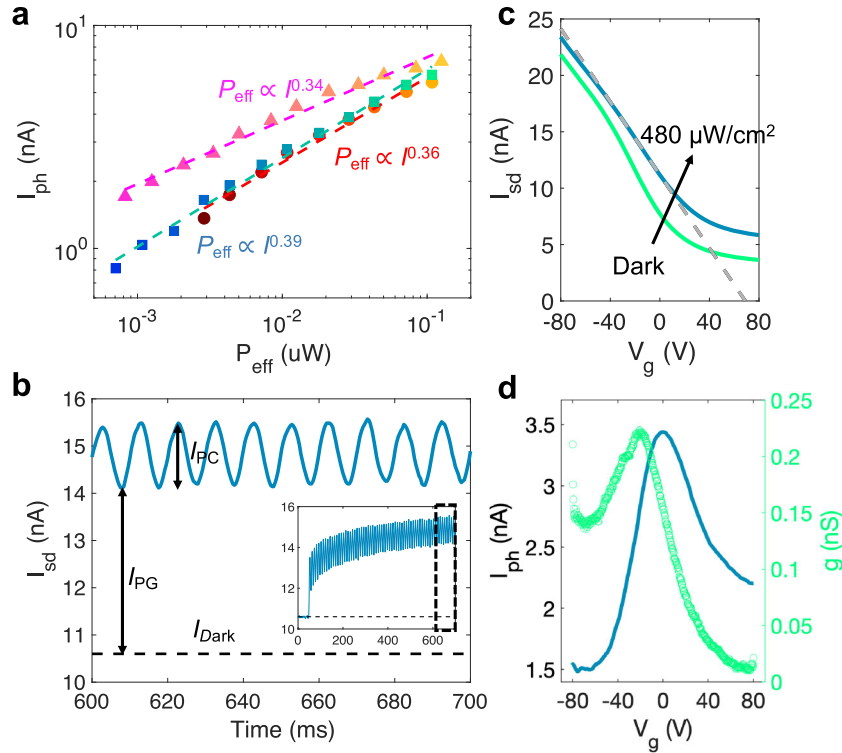


**Fig. 4 Power and gate dependence of photocurrent.** **a** Photocurrent versus effective incident power for excitation energies of 1.98 eV (color gradient in red tone), 2.33 eV (color gradient in green tone), and 3.22 eV (color gradient in magenta tone). The dashed lines are obtained from a linear fit to each data set by following the power-law  $I_{ph} \propto P_{eff}^a$ . **b** Drain current as a function of time under illumination modulated at a frequency of 10 Hz and excitation energy of 2.33 eV and a power density of  $480 \mu\text{W}/\text{cm}^2$ . The horizontal dashed line indicates the amount of drain current in the dark. The inset shows the same drain current on a longer time scale, with a black dashed rectangle indicating the main plot zone. Measurements in **(a, b)** have been performed at  $V_{sd} = 5 \text{ V}$  and  $V_g = 0 \text{ V}$  for device C ( $\sim 40 \text{ nm}$  thick). **c** Transfer curves under dark and illumination (2.33 eV) conditions at  $V_{sd} = 5 \text{ V}$ . The dashed black line is a linear fit to the dark transfer curve, obtaining a  $V_T = 36.9 \text{ V}$ . The calculated shift in threshold voltage when illuminating ( $\Delta V_T = 32.1 \text{ V}$ ) is indicated by a dashed gray line. **d** Device photocurrent (blue line) and transconductance (green dots) obtained from the plot in panel **(c)**. Results in **(c, d)** have been performed for device D ( $\sim 40 \text{ nm}$  thick).

structural and electronic properties of  $\text{FePS}_3$  as a function of the effective  $U$ . The effective  $U$  was applied to the Fe  $d$  orbitals and varied between 0 and 5 eV. The calculated total energy and energy bandgap for each configuration are reported in Supplementary Note 6. As we may observe, both a metallic and an insulating phase could be energetically stabilized, as a consequence of the fascinating correlated electron physics of the system. Indeed, recent works have demonstrated the possibility of driving an insulator-to-metal transition by applying external pressure<sup>28</sup>. For an effective  $U$  value of 2.2 eV, the calculated bandgap matches 1.23 eV, in excellent agreement with our experiments. The corresponding band structure and density of states are reported in Fig. 3c, d. From the orbital projected density of states (see Supplementary Note 6) we can evidence that the electronic states below the Fermi energy correspond to Fe 3d and S 3p orbitals, whereas the ones above  $E_F$  are principally derived from Fe 3d orbitals.

#### Analysis of the photo-response mechanisms in $\text{FePS}_3$

The origin of the photo-response in layered materials is often due to a variety of mechanisms that take place simultaneously, being these the photoconductive effect, photovoltaic effect and thermal mechanisms, such as photo-thermoelectric and bolometric effects<sup>29</sup>. In our experiments, the devices are illuminated as a whole with light spots much larger than their size, where thermal contributions to the photocurrent are expected to cancel<sup>30</sup>.

On the one hand, the photoconductive effect is mediated by extra free carriers generated from photon absorption, creating free

electrons and holes that drift in opposite directions toward the metallic contacts under the application of an external  $V_{sd}$  and thus leading to a net increase of the drain current. A special case of photoconductivity is the photogating effect, where photoexcited charge carriers are trapped in localized states. These trapped states are frequently located in defects that are present in the semiconducting material as well as in its surface, and they act as a local gate modulating the material's resistance. On the other hand, in the photovoltaic effect, photocurrent originates from a built-in potential, typically arising in PN junctions and/or Schottky barriers, which drives photogenerated electrons and holes in opposite directions even without an externally applied bias voltage. A signature of both the photoconductive ( $I_{PC}$ ) and photovoltaic ( $I_{PV}$ ) effects is their linear growth with the incident optical power ( $I_{PC}, I_{PV} \propto P_{eff}^a$ ,  $a = 1$ ), whereas photogating ( $I_{PG}$ ) increases sub-linearly with the excitation power due to its dependence on a limited number of traps ( $I_{PG} \propto P_{eff}^a$ ,  $a < 1$ )<sup>31</sup>.

To discern the origin of the photocurrent in  $\text{FePS}_3$  based devices, power dependence of the photogenerated current at a fixed  $V_{sd} = 5 \text{ V}$  and at zero gate bias has been collected for three different illumination energies: 1.98 eV (625 nm), 2.33 eV (530 nm) and 3.22 eV (385 nm) (Fig. 4a). Here, a similar device to the one analyzed in Fig. 2 has been fabricated (device C). A linear fit of the experimental data to a power law ( $I_{ph} \propto P_{eff}^a$ ) yields values of  $a$  which are below the unit for the full range of energies studied. The sublinear increase of the photocurrent with the effective incident power reveals a dominantly photogating contribution to the total photocurrent generation in our devices.

**Table 1.** Figures of merit of photodetectors based on TMCPs.

Material	Experimental conditions	Responsivity (mA W <sup>-1</sup> )	Rise time (ms)	Cut-off $\lambda$ (nm)	Spectral range	Ref.
40-nm thick FePS <sub>3</sub> (device D)	$V_{sd} = 5$ V, $V_g = 0$ V, $\lambda = 530$ nm, $P = 480$ $\mu$ W cm <sup>-2</sup>	$2.6 \cdot 10^3$	260	1008	UV-VIS-NIR	This work
15-nm thick FePS <sub>3</sub>	$V_{sd} = 0.06$ V, $V_g = -40$ V, $\lambda = 245$ nm, $P = 0.18$ mW cm <sup>-2</sup>	12.3	105	–	UV	10
5-nm thick NiPS <sub>3</sub>	$V_{sd} = 10$ V, $V_g = N.A.$ , $\lambda = 254$ nm, $P = 100$ $\mu$ W cm <sup>-2</sup>	126	3.2	360	UV	9
40-nm thick MnPS <sub>3</sub>	$V_{sd} = 8$ V, $V_g = 70$ V, $\lambda = 365$ nm, $P = 1.5$ $\mu$ W cm <sup>-2</sup>	$2.88 \cdot 10^5$	340	413	UV	8

This assumption is also supported by the trend of the photocurrent upon modulation of a LED excitation (Fig. 4b). Here, we observe a strong, slow response as part of a background photocurrent and, overlapping, a faster photo-response that oscillates with the modulation frequency. We attribute the slow photo-response contribution to the photogating effect, limited by the recombination lifetime of long-lived trapped states, while the faster photo-response is due to an intrinsic photoconductive effect. The ratio of the two signals ( $R_{slow}/R_{fast} \approx 2.8$ ) highlights the prevalence of the slow photogating response over the faster photoconductive contribution. The lack of any significant contribution to the photocurrent at zero applied source-drain voltage in both scanning photocurrent maps (Supplementary Note 7) and  $I_{sd}$ - $V_{sd}$  measurements under illumination (Supplementary Note 8) discards a photovoltaic origin of the fast component of the photo-response.

The predominantly photogating effect of the photocurrent is also confirmed by the dependence on applied back-gate voltage to a similar device (device D, Fig. 4c). The device threshold voltage ( $V_T = 36.9$  V) has been extracted from a linear fit to the central region of the transfer curve under dark conditions. Under illumination,  $V_T$  shifts to a larger voltage ( $V_T + \Delta V_T = 69$  V). This change in threshold voltage under optical illumination induces an increase in drain current which is directly related to the photogating effect:  $I_{PV} \approx g \cdot \Delta V_T$ , where  $g$  is the transconductance<sup>32</sup>. A qualitative comparison between the total device photocurrent, obtained by subtracting the dark curve to the illuminated one, and the device transconductance, obtained as  $dI_{sd}/dV_g$ , shows that the trend followed by the transconductance and the total photocurrent are similar (Fig. 4d). The shift between the two signals could be related to the hysteretic behavior of devices with gate voltage application (see Supplementary Note 9). With all together, we conclude that the origin of the photocurrent in the devices is a combination of photogating and photoconductive effects, where photogating prevails over the intrinsic photoconductive mechanism.

To put into context the performance of our FePS<sub>3</sub> based devices, a comparative table with the most critical parameters of 2D photodetectors based on other TMCPs is shown (Table 1). The experimental conditions are also included for a fair comparison. Compared to other devices based on other TMCPs such as MnPS<sub>3</sub> and NiPS<sub>3</sub>, our FePS<sub>3</sub> based devices offer fewer limitations in the detection range, being a narrow bandgap semiconductor and exhibiting a large cut-off wavelength (1008 nm) with a broader spectral response from UV to NIR. The response time of FePS<sub>3</sub> devices presents similar order of magnitude as other typical 2D photodetectors<sup>33</sup>. All the features displayed by FePS<sub>3</sub> nanosheets make it a good candidate for broadband electrical detection of optical excitations at the nanoscale, offering sensitivity at spectral ranges that are unattainable with devices based on TMDCs as active materials<sup>33,34</sup>.

### Stability of FePS<sub>3</sub> under ambient conditions

After a complete optical, electrical, and optoelectronic characterization of the FePS<sub>3</sub> sheets, the stability of the flakes under ambient conditions has been studied. During the experiments carried out in this work, we observed a small decrease of the optoelectronic response over weeks for devices exposed to air. This, together with the lack of conduction of devices prepared out of flakes thinner than 20 nm and the surface spots visible in the AFM images (Fig. 1c), points toward degradation of the outermost layers of the material when exposed to air, that eventually results in the change of appearance of bulk crystals after long exposures (Supplementary Note 10).

In order to carefully characterize this possible aging of the material, thin FePS<sub>3</sub> flakes have been mechanically exfoliated and deposited onto a transparent Gel-Film substrate. We tracked the

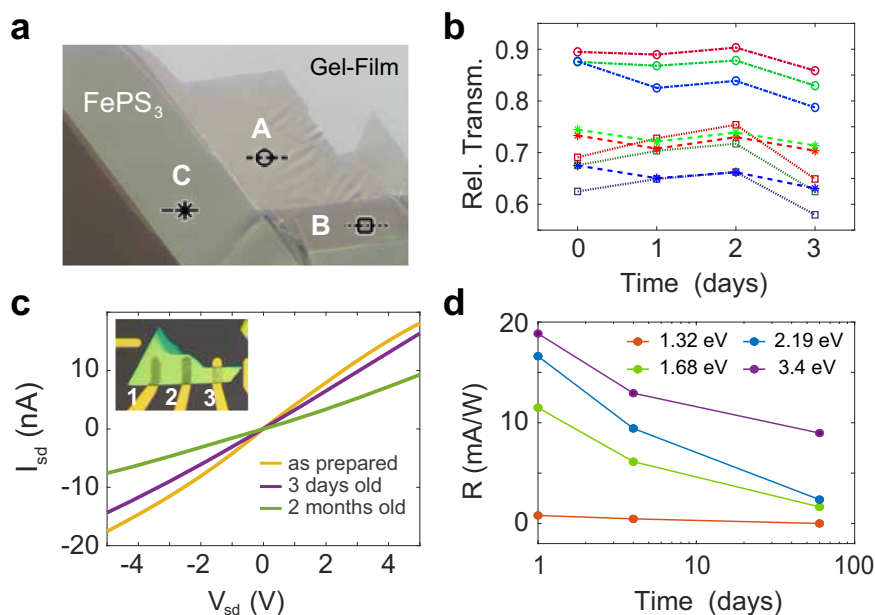


**Fig. 5 Time evolution of the optoelectronic properties.** **a** Transmission optical microscope image of FePS<sub>3</sub> exfoliated flake onto a Gel-Film polymeric substrate. The white scale bar represents 10  $\mu\text{m}$ . Three zones (A–C) with an estimated thickness of 15, 30, and 85 nm, respectively, are selected for transmission measurements over time. **b** Flake transmission relative to the substrate at the A–C zones labeled in panel (a) for the R, G, and B CMOS channels. **c**  $I$ – $V$  characteristics of the same 30-nm thick FePS<sub>3</sub> flake presented in Fig. 2 as a function of time. Two-terminal measurements were performed between contacts 1–2, as labeled in the flake image in the inset. **d** Time evolution of the device responsivity as a function of energy.

**Table 2.** Transmission reduction of FePS<sub>3</sub> flakes preserved under ambient conditions for each RGB channel and measured at “day 3” relative to “day 0”.

	Red (%)	Green (%)	Blue (%)
Zone A	4	5	10
Zone B	4	4	7
Zone C	6	8	7

evolution of the relative transmittance over time for flakes of different thickness exposed to ambient conditions. Typical aging mechanisms, such as oxidation, etching, or change in chemical composition are expected to sensibly modify the transmission of the flakes. Microscope inspection of the flakes exposed to air after several hours does not reveal any preliminary sign of material degradation since the flakes preserve the transmittance even for the case of ultrathin material (<10 nm). In Fig. 5a, b, we present the data for three different areas of a flake (A–C) of approximately 15, 30, and 85 nm thickness, respectively. Except for minor fluctuations, the relative transmittance remains constant throughout the two first days from the flake’s exfoliation for the three zones selected. The first change in flake’s transmission occurs three days after preparation when a noticeable reduction of about 5–10% in the relative transmittance is observed for all zones of the flake. These results are summarized in Table 2.

We attribute the reduction in transmission of FePS<sub>3</sub> flakes with a loss in the transparency of the most external layers of material, where the nanosheet surface can react with air and consequently resulting in a gain of material’s opacity with time (see Supplementary Note 10). The flakes have also been exposed to white light and UV illumination during two days from the exfoliation day. No variations in the relative transmittance of the nanosheets with respect to the aging experiments performed in dark are observed, concluding that the aging of the flakes is not due to any photo-induced mechanism. This is in contrast with

other 2D materials, such as CrI<sub>3</sub> which represents a strong degradation under optical illumination<sup>35</sup>.

Possible changes in the electronic and optoelectronic properties of FePS<sub>3</sub> nanosheets over time have been also studied under ambient atmosphere. In this case, the 30-nm thick device characterized in Fig. 2 has been used to study the electrical as well as the optoelectronic aging of the material. Figure 5c shows an  $I$ – $V$  curve at zero gate bias conducted at three different moments in time: right after the device was fabricated, 3 days later and 2 months from its fabrication. The device was kept in the air during the time interval between consecutive measurements. The  $I_{\text{sd}}$ – $V_{\text{sd}}$  plot reveals a decrease in the electrical conductivity of the FePS<sub>3</sub> flake along time, reaching half of the original value after a period of 2 months. We attribute this reduction in flake conductivity to possible oxidation of the outermost layers that are in contact with air. This hypothesis is supported by the lack of conductivity in a device made from a 10-nm thick FePS<sub>3</sub> flake exfoliated in the air.

The evolution in time of the photo-response of the same 30-nm thick FePS<sub>3</sub> device is summarized in Fig. 5d. Similar to optical transmittance and electronic transport measurements, the optoelectronic features of the FePS<sub>3</sub> device are also affected over time, resulting in a notable decrease of more than 50% of the original responsivity after two months from the fabrication of the device. Nevertheless, compared to phosphorene and other 2D materials, which show a high reactivity with oxygen and water and suffer a fast degradation under ambient conditions in just a few hours<sup>36</sup>, FePS<sub>3</sub> nanosheets exhibit fairly high stability in air. This peculiarity contributes to the development of future long-lasting broadband photodetectors with FePS<sub>3</sub> as a very promising material.

In summary, we have investigated aspects of the optical and optoelectronic properties of few-layered FePS<sub>3</sub> which remained, to our knowledge, partially or fully unexplored. From a meticulous study at room temperature of the optical transmittance of the material as a function of thickness we first provide a reference guideline for thickness identification of FePS<sub>3</sub> nanosheets by means of simple optical transmission microscopy

imaging. These results allow us also to estimate the refractive index of the material, a parameter that plays an important role in the design of future optical and optoelectronic nanostructures integrating FePS<sub>3</sub> nanosheets. Also, being a p-type semiconductor—a fact that we confirm in the electrical characterization of FePS<sub>3</sub> field-effect devices—makes FePS<sub>3</sub> an interesting material for the study of proximity effects in stacked p–n heterostructures. From the photo-response of the FePS<sub>3</sub> devices, we determine the bandgap energy of the material, and more importantly, we demonstrate a wide spectral response to optical excitation for FePS<sub>3</sub>, ranging from the near IR up to the UV energy regions. Hubbard-corrected ab-initio DFT + *U* calculations corroborate our experimental results. The trend of photocurrent with incident power and applied gate voltage suggests a scenario dominated by photogating effects. To reinforce the device's suitability for optoelectronic applications we show that it suffers minimal deterioration over long time exposure to ambient conditions. Our results indicate that FePS<sub>3</sub> is a good candidate material for applications in optoelectronics, owing to a narrow gap and a broad photo-response, in contrast with TMDC materials that can be exclusively used within the visible spectral region; in addition, it offers better environmental stability than other 2D materials with a similar spectral response. Finally, a fundamental understanding of the photoconductive properties of FePS<sub>3</sub> paves the way toward exploring exciting magneto-optical tunability or spintronic effects in its magnetic phase at low temperatures. The peculiarity of its resilience under exposure to light and environmental conditions brings FePS<sub>3</sub> to the spotlight of 2D intrinsic magnetic materials; when compared to the renowned CrI<sub>3</sub>, which exhibits extreme instability under similar conditions, FePS<sub>3</sub> becomes an advantageous material for fast and simple testing.

## METHODS

### Material synthesis

FePS<sub>3</sub> crystals were grown by chemical vapor transport, using iodine as a transport agent, and characterized by powder X-ray diffraction and ICP-OES (Inductively Coupled Plasma–Optical Emission Spectrometry), as previously reported<sup>37</sup>.

### The build-up of the material thickness identification guideline

The FePS<sub>3</sub> nanosheets were isolated through mechanical exfoliation of the synthesized FePS<sub>3</sub> bulk crystal with Nitto SPV 224 tape and deposited onto transparent Gel-Film (Gel-Pak, WF x4 6.0 mil) substrate for inspection under an optical microscope. Transmission mode optical images of the flakes on Gel-Film were recorded with a metallurgical microscope (Motic BA310 Met-T) equipped with a digital CMOS Camera (AMScope MU1803 with sensor Aptina AR1820). Right after the transmittance characterization, the transparency of the Gel-Film substrate allowed for a deterministic dry transfer<sup>38</sup> of the optically characterized FePS<sub>3</sub> nanosheets onto a SiO<sub>2</sub>/Si substrate, where AFM was employed to identify the thickness of the flakes. Note that AFM imaging on the surface of Gel-Film results is challenging because of its high compliance. Following this methodology, the acquisition of optical transmission images and AFM maps of several flakes with a thickness in the range of 4–100 nm allowed the build-up of the thickness identification guide.

### Optoelectronic characterization

The bench of fiber-coupled LEDs used to characterize the response to light of the nanodevices was selected from Thorlabs, offering different photon energies from NIR (1.32 eV) up to UV (3.40 eV) with emission bandwidths around 10–20 nm and reaching maximum optical powers at about 10–15 mW at the output of a coupled 400 μm-core fiber. The use of a focusing lens after the fiber output enabled to focus the LED light down to a 600 μm-diameter spot onto the device. A smaller spectral range but higher resolution was achieved at energies near the optical gap of FePS<sub>3</sub> using a high power tuneable light source (TLS120Xe, Bentham) offering 0.0035 nm of wavelength resolution.

Frequency modulation of the illumination source during electrical current measurements was performed with an external function generator (FG420, Yokogawa) connected to a LED driver (LEDD1B, Thorlabs).

### Electronic structure calculations

The generalized gradient approximation (GGA) and the Perdew–Burke–Ernzerhof functional<sup>39</sup> were used to describe the exchange–correlation energy. Standard solid state pseudopotentials precision pseudopotentials from the Materials Cloud database<sup>40</sup> were selected and the electronic wave functions were expanded with well-converged kinetic energy cut-offs of 90 and 1080 Ry for the wave functions and charge density, respectively. All the structures were fully optimized without constraints until the forces on each atom were smaller than 10<sup>−4</sup> Ry/au and the energy difference between two consecutive relaxation steps was less than 2 × 10<sup>−4</sup> Ry. The Brillouin zone was sampled by a very fine (0.15 Å<sup>−1</sup> k-points distance)  $\Gamma$  centered 8 × 5 × 7 k-point Monkhorst–Pack mesh<sup>41</sup> for all calculations. In order to describe the strong correlation of the electrons in Mott–Hubbard physics, we adopted a DFT + *U* approach, where *U* is the on-site Coulomb repulsion, using the simplified version proposed by Dudarev et al.<sup>42</sup>. Spin–orbit coupling effects were also taken into account using fully relativistic norm-conserving pseudopotentials from Pseudo Dojo<sup>43</sup>, showing no significant variations (Supplementary Note 6). Dispersion corrections to account for van der Waals interactions between the FePS<sub>3</sub> layers were considered by applying semi-empirical Grimme-D2 corrections<sup>44</sup>.

### DATA AVAILABILITY

The datasets generated during and/or analyzed during the current study are available from the corresponding author on reasonable request. All data generated or analyzed during this study are included in this published article and its Supplementary Information.

Received: 12 June 2020; Accepted: 11 January 2021;

Published online: 15 February 2021

## REFERENCES

- Novoselov, K. S. et al. Electric field effect in atomically thin carbon films. *Science* **306**, 666–669 (2004).
- Splendiani, A. et al. Emerging photoluminescence in monolayer MoS<sub>2</sub>. *Nano Lett.* **10**, 1271–1275 (2010).
- Wang, G. et al. Colloquium: excitons in atomically thin transition metal dichalcogenides. *Rev. Mod. Phys.* **90**, 021001 (2018).
- Lopez-Sanchez, O., Lembke, D., Kayci, M., Radenovic, A. & Kis, A. Ultrasensitive photodetectors based on monolayer MoS<sub>2</sub>. *Nat. Nanotech.* **8**, 497–501 (2013).
- Dhanabalan, S. C., Ponraj, J. S., Zhang, H. & Bao, Q. Present perspectives of broadband photodetectors based on nanobelts, nanoribbons, nanosheets and the emerging 2D materials. *Nanoscale* **8**, 6410–6434 (2016).
- Konstantatos, G. Current status and technological prospect of photodetectors based on two-dimensional materials. *Nat. Commun.* **9**, 5266 (2018).
- Du, K. et al. Weak van der Waals stacking, wide-range band gap, and Raman study on ultrathin layers of metal phosphorus trichalcogenides. *ACS Nano* **10**, 1738–1743 (2016).
- Kumar, R., Jenjeti, R. N., Austeria, M. P. & Sampath, S. Bulk and few-layer MnPS<sub>3</sub>: a new candidate for field effect transistors and UV photodetectors. *J. Mater. Chem. C* **7**, 324–329 (2019).
- Chu, J. et al. High-performance ultraviolet photodetector based on a few-layered 2D NiPS<sub>3</sub> nanosheet. *Adv. Funct. Mater.* **27**, 1701342 (2017).
- Gao, Y. et al. Bias-switchable negative and positive photoconductivity in 2D FePS<sub>3</sub> ultraviolet photodetectors. *Nanotechnology* **29**, 244001 (2018).
- Brec, R., Schleich, D. M., Ouvrard, G., Louisy, A. & Rouxel, J. Physical properties of lithium intercalation compounds of the layered transition-metal chalcogenophosphites. *Inorg. Chem.* **18**, 1814–1818 (1979).
- Kurosawa, K., Saito, S. & Yamaguchi, Y. Neutron diffraction study on MnPS<sub>3</sub> and FePS<sub>3</sub>. *J. Phys. Soc. Jpn.* **52**, 3919–3926 (1983).
- Jernberg, P., Bjarman, S. & Wäppling, R. FePS<sub>3</sub>: a first-order phase transition in a “2D” Ising antiferromagnet. *J. Magn. Magn. Mater.* **46**, 178–190 (1984).
- Wang, X. et al. Raman spectroscopy of atomically thin two-dimensional magnetic iron phosphorus trisulfide (FePS<sub>3</sub>) crystals. *2D Mater.* **3**, 031009 (2016).
- Lee, J. U. et al. Ising-type magnetic ordering in atomically thin FePS<sub>3</sub>. *Nano Lett.* **16**, 7433–7438 (2016).



16. Nēmec, P., Fiebig, M., Kampfrath, T. & Kimel, A. V. Antiferromagnetic spintronics. *Nat. Phys.* **14**, 229–241 (2018).
17. Burch, K. S., Mandrus, D. & Park, J. G. Magnetism in two-dimensional van der Waals materials. *Nature* **563**, 47–52 (2018).
18. Shabbir, B. et al. Long range intrinsic ferromagnetism in two dimensional materials and dissipationless future technologies. *Appl. Phys. Rev.* **5**, 041105 (2018).
19. Taghavi, N. S. et al. Thickness determination of MoS<sub>2</sub>, MoSe<sub>2</sub>, WS<sub>2</sub> and WSe<sub>2</sub> on transparent stamps used for deterministic transfer of 2D materials. *Nano Res.* **12**, 1691–1695 (2019).
20. Born, M. & Wolf, E. *Principles of Optics: Electromagnetic Theory Of Propagation, Interference and Diffraction of Light*. (Pergamon, Oxford; New York, 1980).
21. Cardenas-Valencia, A. M., Dlutowski, J., Fries, D. & Langebrake, L. Spectrometric determination of the refractive index of optical wave guiding materials used in lab-on-a-chip applications. *Appl. Spectrosc.* **60**, 322–329 (2006).
22. Frindt, R. F., Yang, D. & Westreich, P. Exfoliated single molecular layers of Mn<sub>0.8</sub>PS<sub>3</sub> and Cd<sub>0.8</sub>PS<sub>3</sub>. *J. Mater. Res.* **20**, 1107–1112 (2005).
23. Aruchamy, A., Berger, H. & Levy, F. Photoelectric properties of the p-type layered trichalcogenophosphates FePS<sub>3</sub> and FePSe<sub>3</sub>. *J. Solid State Chem.* **72**, 316–323 (1988).
24. Li, X., Cao, T., Niu, Q., Shi, J. & Feng, J. Coupling the valley degree of freedom to antiferromagnetic order. *Proc. Natl Acad. Sci. USA* **110**, 3738–3742 (2013).
25. Li, Y. et al. High performance broadband photo and soft X-ray detectors based on two dimensional CrSiTe<sub>3</sub>. *J. Mater. Chem. C* **8**, 6659–6666 (2020).
26. Ou, Z. et al. Enabling and controlling negative photoconductance of FePS<sub>3</sub> nanosheets by hot carrier trapping. *Adv. Opt. Mater.* **8**, 2000201 (2020).
27. Giannozzi, P. et al. Quantum Espresso: a modular and open-source software project for quantum simulations of materials. *J. Phys. Condens. Matter* **21**, 395502 (2009).
28. Haines, C. R. S. et al. Pressure-induced electronic and structural phase evolution in the van der Waals compound FePS<sub>3</sub>. *Phys. Rev. Lett.* **121**, 266801 (2018).
29. Buscema, M. et al. Photocurrent generation with two-dimensional van der Waals semiconductors. *Chem. Soc. Rev.* **44**, 3691–3718 (2015).
30. Island, J. O., Blanter, S. I., Buscema, M., van der Zant, H. S. & Castellanos-Gomez, A. Gate controlled photocurrent generation mechanisms in high-gain In<sub>2</sub>Se<sub>3</sub> phototransistors. *Nano Lett.* **15**, 7853–7858 (2015).
31. Sze, S. M. & Ng, K. K. *Physics of Semiconductor Devices*. (John Wiley & Sons, Hoboken, NJ, 2006).
32. Furchi, M. M., Polyushkin, D. K., Pospischil, A. & Mueller, T. Mechanisms of photoconductivity in atomically thin MoS<sub>2</sub>. *Nano Lett.* **14**, 6165–6170 (2014).
33. Choi, W. et al. High-detectivity multilayer MoS<sub>2</sub> phototransistors with spectral response from ultraviolet to infrared. *Adv. Mater.* **24**, 5832–5836 (2012).
34. Perea-López, N. et al. Photosensor device base don few-layered WS<sub>2</sub> films. *Adv. Funct. Mater.* **23**, 5511–5517 (2013).
35. Shcherbakov, D. et al. Raman spectroscopy, photocatalytic degradation, and stabilization of atomically thin chromium tri-iodide. *Nano Lett.* **18**, 4214–4219 (2018).
36. Castellanos-Gomez, A. et al. Isolation and characterization of few-layer black phosphorus. *2D Mater.* **1**, 025001 (2014).
37. Šiškins, M. et al. Magnetic and electronic phase transitions probed by nano-mechanical resonators. *Nat. Commun.* **11**, 2698 (2020).
38. Castellanos-Gomez, A. et al. Deterministic transfer of two-dimensional materials by all-dry viscoelastic stamping. *2D Mater.* **1**, 011002 (2014).
39. Perdeew, J. P., Burke, K. & Ernzerhof, M. Generalized gradient approximation made simple. *Phys. Rev. Lett.* **77**, 3865 (1996).
40. Prandini, G., Marrazzo, A., Castelli, I. E., Mounet, N. & Marzari, N. Precision and efficiency in solid-state pseudopotential calculations. *npj Comput. Mater.* **4**, 72 (2018).
41. Monkhorst, H. J. & Pack, J. D. *Phys. Rev. B* **13**, 5188 (1976).
42. Dudarev, S. L., Botton, G. A., Savrasov, S. Y., Humphreys, C. J. & Sutton, A. P. *Phys. Rev. B* **57**, 1505 (1998).
43. Van Setten, M. J. et al. The PseudoDojo: training and grading a 85 element optimized norm-conserving pseudopotential table. *Comput. Phys. Commun.* **226**, 39 (2018).

44. Grimme, S. Semiempirical GGA-type density functional constructed with a long-range dispersion correction. *J. Comput. Chem.* **27**, 1787–1799 (2006).

## ACKNOWLEDGEMENTS

The present work has received funding from the European Union's Horizon 2020 research and innovation program through the European Research Council grants ERC-2017-StG-755655 2D-TOPSENSE, ERC-2018-AdG-788222 MOL-2D, under the Graphene Flagship through projects GrapheneCore2 (grant nr. 785219), and GrapheneCore3 (grant nr. 881603) and through the COST Action CA15128 MOLSPIN. The authors also acknowledge funding from the Spanish Government through the Unit of Excellence "María de Maeztu" MDM-2015-0538, through projects MAT2017-88377-C2-2-R (AEI/FEDER), MAT2017-88377, MAT2017-89528 (AEI/FEDER), and R.F.'s Juan de la Cierva-formación fellowship FJCI-2017-32919. This work has been supported by the Generalitat Valenciana, through grants CIDEAGENT/2018/004, CIDEAGENT/2018/005, CIDEAGENT/2019/022, the Prometeo Program of Excellence, and M.R.'s APOSTD/2020/249 fellowship.

## AUTHOR CONTRIBUTIONS

FePS<sub>3</sub> crystals were synthesized and characterized by S.M.V. and E.C. FePS<sub>3</sub> flakes were prepared, characterized, and devices fabricated by M.R., F.C., R.F., and P.G. The electrical and optoelectronic characterization was performed by M.R. and F.C., data analysis was carried out by M.R. and M.R.C., and ab initio calculations were performed by D.L.E. and J.J.B. This work was conceived and drafted by M.R., A.C.G., and M.R.C. All authors contributed to the interpretation of results and final elaboration of the paper.

## COMPETING INTERESTS

The authors declare no competing interests.

## ADDITIONAL INFORMATION

**Supplementary information** The online version contains supplementary material available at <https://doi.org/10.1038/s41699-021-00199-z>.

**Correspondence** and requests for materials should be addressed to M.R., A.C.-G. or M.R.C.

**Reprints and permission information** is available at <http://www.nature.com/reprints>

**Publisher's note** Springer Nature remains neutral with regard to jurisdictional claims in published maps and institutional affiliations.



**Open Access** This article is licensed under a Creative Commons Attribution 4.0 International License, which permits use, sharing, adaptation, distribution and reproduction in any medium or format, as long as you give appropriate credit to the original author(s) and the source, provide a link to the Creative Commons license, and indicate if changes were made. The images or other third party material in this article are included in the article's Creative Commons license, unless indicated otherwise in a credit line to the material. If material is not included in the article's Creative Commons license and your intended use is not permitted by statutory regulation or exceeds the permitted use, you will need to obtain permission directly from the copyright holder. To view a copy of this license, visit <http://creativecommons.org/licenses/by/4.0/>.

© The Author(s) 2021